3-D X-ray nanotomography of cells grown on electrospun scaffolds

Robert S. Bradley[1,3]**, Ian K. Robinson**[2,3] **and Mohammed Yusuf**[2,3]

[1]*Henry Moseley X-ray Imaging Facility, The University of Manchester, UK*

[2]*London Centre for Nanotechnology, University College London, London, UK*

[3]*Research Complex at Harwell, Rutherford Appleton Laboratory, Oxon, UK*

Abstract

We demonstrate that x-ray nanotomography with Zernike phase contrast can be used for 3-D imaging of cells grown on electrospun polymer scaffolds. The scaffold fibres and cells are simultaneously imaged, enabling the influence of scaffold architecture on cell location and morphology to be studied. The high resolution enables subcellular details to be revealed. The x-ray imaging conditions were optimised to reduce scan times, making it feasible to scan multiple regions of interest in relatively large samples. An image processing procedure is presented which enables scaffold characteristics and cell location to be quantified. The procedure is demonstrated by comparing the ingrowth of cells after culture for 3 days and 6 days.

1. Introduction

Tissue engineering aims to recover the function of damaged tissues and organs by combining techniques from life sciences and engineering. A key strategy is to develop implantable 3-D scaffolds onto which cells are seeded and grown. The scaffolds must provide analogous functions to that of the extra-cellular matrix of the target tissue, which is achieved by designing a structure with suitable architecture, mechanical properties, cyto-compatibility, and bioactivity [1]. Scaffold architecture is important in achieving good cell adhesion and hence high cell seeding efficiencies, with porosity and surface area to volume ratio being key characteristics [2,3]. Pore space diameter and pore connectivity are important for tissue-ingrowth and vascularisation [3].

Imaging plays an important role in assessing these characteristics and in the understanding the growth of cells in scaffolds. 3-D quantitative information can be obtained on scaffold architecture, including how it changes over time, and on cell infiltration and differentiation. Appel *et al.* [4] reviewed 3-D imaging approaches for tissue engineering applications and highlighted the need for further technique development to address all imaging requirements. State of the art optical imaging techniques, such as multi-photon laser confocal fluorescence microscopy (LSCM) and light sheet microscopy, are being increasingly used and can provide 3-D information at spatial resolutions down to ~0.2 µm for relatively thick but translucent specimens [5]. The information revealed however is sparse, in that only fluorescently labelled structures are imaged, while the spatial resolution is typically not isotropic and the signal-to-noise ratio decreases with depth. Furthermore, high light intensities are often required which can lead to fluorophore bleaching and phototoxic effects [5]. At higher resolution, destructive imaging techniques such as FIB-SEM can be used, which are particularly suited to analysing

cell interactions with nanostructured scaffolds [6-8]. However FIB-SEM has a limited field of view and is suited to imaging near surface features.

High resolution x-ray tomography is a promising alternative for non-destructive 3-D imaging at resolutions from tens of microns to tens of nanometres [9]. X-ray absorption provides excellent contrast for hard tissues and microCT is being widely adopted for studying osteogenesis in bone constructs [10-12]. However, absorption contrast is poor for soft tissues and light materials such as polymer scaffolds. Contrast agents can be used to improve x-ray absorption. For example, phosphotungstic acid and iodine based stains have been used to visualise and characterise *in-vitro* engineered extracellular matrix [13], while osmium tetroxide has been used to stain cells seeded on polymer scaffolds [14,15]. Zehbe *et al.* [16] used a combined Au /Ag stain to image chondrocytes seeded on gelatine scaffolds, while Thimm *et al.* [17] used targeted FeO particles to label endothelial cells in polyurethane scaffolds. However it may be difficult to achieve uniform staining across a sample (particularly for small pore scaffolds) [16,18] and non-specific staining can reduce sensitivity. For example, Dorsey *et al.* [14] concluded that microCT was 5 times less sensitive for detecting cells than a DNA assay and is hence limited to quantifying cell densities greater than a million cells / ml.

Phase contrast imaging techniques can overcome these limitations of absorption contrast by generating contrast from the real part of the object's refractive index, which can be 1000 times greater at hard x-ray energies than the real part which gives rise to absorption [9]. There is a variety of x-ray phase imaging techniques being actively developed. At the micron resolution scale, phase contrast imaging has been used to visualise the microstructure of polymer and gelatine scaffolds [19-21] as well as their degradation after implantation [22]. Recently, Hagen *et al.* [23] compared different phase contrast techniques for imaging the microstructure of decelluarlised tissues. At higher resolutions, Zernike phase contrast and coherent diffraction imaging have been used to image single cells or clusters of cells with sub-cellular detail [24-27].

In this paper, we demonstrate that laboratory x-ray phase contrast nanotomography can be used to image cells, with subcellular detail, seeded on polymer scaffolds whilst also providing key information on both cell location and scaffold architecture. The linking together of 3-D information on both cells and scaffolds has the potential to provide new insights into cyto-compatibility and bioactivity. The x-ray imaging conditions were optimised to enable lower dose, higher throughput region-of-interest scanning of relatively large specimens. An image processing procedure has been developed to enable scaffold characteristics and cell location to be quantified. The procedure is demonstrated by comparing cell infiltration into polymer scaffolds after culture for 3 days and 6 days.

2. Materials and methods
2.1. Sample preparation

Samples were prepared using the protocols described in [28,29]. Briefly, electrospun poly(lactide-co-glycolide) (PLGA) scaffolds with fibre diameter of ~4 μm and thickness of ~70 μm were obtained from the Electrospinning Company, UK. Cell culture using human fibroblast cells was carried out for 3 days and 6 days. Scaffolds containing cells were then fixed using 2.5% (vol/vol) glutaraldehyde in 0.1 M cacodylate buffer (pH 7.2) for 2 hours. Samples were then washed three times with 0.1 M cacodylate buffer (pH 7.2), dehydrated

using a series of ethanol solutions (70%, 85%, and 100%), and finally dried using Hexamethyldisilazane (HMDS) (Sigma Aldrich, UK) for 5 min.

2.2. X-ray nanotomography

Sections of the scaffolds of ~200-500 μm in width were prepared mechanically and placed within 1 mm diameter kapton tubing for x-ray scanning. The samples were scanned using a Zeiss Xradia Ultra-810 system using the 150 nm resolution optics with Zernike phase contrast [30]. The system is a zone plate transmission x-ray microscope with a 65 μm field of view and uses quasi-monochromatic x-rays with energy of 5.4 keV. A schematic diagram of the system is shown is Figure 1. The scaffolds were however found to be sensitive to x-ray dose, with long scans (~8 hours) leading with damage of the fibres. The scan settings were therefore optimised to reduce dose while maintaining an acceptable contrast to noise ratio. The exposure time was set to 10 s per radiograph and 541 radiographs were taken over 180º, giving a scan time of ~1 hour 37 minutes. Volumetric data was reconstructed with a voxel size of 127 nm using filtered-back projection.

Two overlapping scans were taken at each region-of-interest (ROIs) to image the full thickness of the scaffold and the volumetric data stitched together after reconstruction. Further details are given in the image analysis section.

Scans were taken at 3 regions-of-interest (ROIs) for 2 scaffold sections prepared from the same sample at each time point, giving 6 ROIs in total for each of the 3 day and 6 day time points. The total scaffold volume sampled per time point was ~2.5 x 10^6 μm^3.

2.3. Image analysis

A semi-automatic image processing procedure was developed to aid visualisation and enable quantification of scaffold characterisation as well as the infiltration of the cells into the scaffold. The procedure comprised the following 6 stages:

1. Stitching of data sets

The two overlapping scans per ROI were stitched together by first aligning the data automatically using the image processing toolbox in Matlab 2014a (Mathworks, Natick, MA). The grey levels of the two volumes in the overlap region were matched prior to stitching by finding the linear transform of the data in one scan which led to the best agreement between the grey level cumulative density functions. The data from the two scans in the overlap region were then averaged, as shown in Figure 2(a).

2. Removal of the phase contrast artefacts

The Zernike method of phase contrast imaging typically gives rise to halo artefacts at the edges of features [30]. While these artefacts aid feature detection, they can make segmentation more difficult. Therefore, an image filter was developed to remove the phase contrast artefacts inspired by the model of Zernike phase contrast for optical microscopes by Yin *et al.* [31]. In this model the artefacts in the 2-D optical images are given by a convolution kernel applied to artefact-free images, where the kernel involves an obscured Airy function (difference between Bessel's functions). We propose the following simpler 3-D convolution kernel which gives rise to the artefacts in the tomographic reconstructed slices:

$$F(\mathbf{r}) = A\delta(\mathbf{r}) + B\,\mathrm{DoG}(\mathbf{r}, \sigma_1, \sigma_2) \qquad\qquad (1)$$

where $\mathbf{r}$ is position, δ is the delta function and DoG is the difference between two 3-D Gaussians with mean zero and isotropic standard deviations, σ_1 and σ_2. Deconvolution with the above kernel then gives volumetric data with the artefacts removed or reduced. Total variation regularisation was used for the deconvolution, via the approach of Chan *et al*. [32], in order to reduce the effects of noise.

Suitable values of the standard deviations (σ_1 and σ_2) and constants (A and B) were obtained via an optimization approach. An ROI containing a single scaffold fibre was selected and the fibre segmented. The segmentation was convolved with the proposed filter (which was evaluated on a 7 x 7 x 7 grid) to simulate data with Zernike artefacts. The parameters were then optimised so that the simulated artefact data was in good agreement (in terms of least squared difference) with the acquired tomographic data for that ROI.

For the total variation (TV) deconvolution, the amount of regularisation was controlled by a single parameter, whose values was chosen as a compromise between artefact removal and noise propagation, and was kept constant for all data sets. Examples of reconstructed slices before and after artefact reduction are shown in Figure 2.

3. Segmentation of the scaffold fibres

Segmentation of the fibres was based on identifying structures with a local thickness similar in value to the known fibre diameter of ~4 μm. First a grey level threshold was applied to segment both cells and fibres, with opening and closing morphological operations applied to remove small islands. The 3-D local thickness was then calculated using ImageJ [33] and hysteresis thresholding was applied to the thickness data to preferentially select the fibres. An example slice through the local thickness data is given in Figure 3(a). Manual adjustment was carried out as necessary to remove any remaining regions corresponding to cells or background.

4. Segmentation of the cells

2-D region growing was applied slice by slice to segment the cells in the regions from step 3 identified as not corresponding to fibres. For quantification of cell infiltration, this procedure was carried out on every 10th slice in order to reduce processing time.

5. Quantifying the distance of cells from the upper scaffold surface

The upper surface of the scaffold (the surface on which cells were seeded) was determined by fitting a 2-D plane to the upper most voxels of the fibre segmentation. The volumetric data were split into a 5 x 5 grid along the 2 axes that were approximately parallel to the scaffold surface, and the fibre voxel in each grid with the minimum z coordinate (along the scaffold depth direction) was identified. A plane was then fitted to the coordinates of these 25 voxels using the RANSAC algorithm, using the Matlab code available from http://www.peterkovesi.com/matlabfns/index.html. An example of a fitted plane is given in Figure 3(b). The depth of each cell voxel was then calculated as the perpendicular distance away from the upper plane. The same procedure was adapted to find the lower scaffold surface and the mean distance between planes was used as a measure of scaffold thickness.

However, the number of voxels, $N(d)$, sampled as a function of distance, d, from the scaffold surface is non-uniform as the stitched data comprises two overlapping cylinders (see Figure 2). Therefore, when calculating the histograms of cell volume as a function of distance, the distribution for each ROI was weighted by $N_{max}/N(d)$, where N_{max} is the maximum value of N over all d and all ROIs. This weighting also accounts for any differences between the total volume scanned for the 3 day and 6 day time points.

    6.   Quantifying scaffold and cell characteristics

Scaffold architecture was characterised in terms of porosity, pore size and fibre diameter from sub-regions within each ROI. Pore size was determined using the local thickness measure [34], while fibre diameter was determined by first skeletonising the fibre segmentation, using the autoskeleton module in Avizo 9 (FEI VSG, Burlington, MA), and then calculating the modal diameter measure given in [35]. The modal diameter is calculated for every point on the skeleton as the diameter about the skeleton position, and in a plane perpendicular to the local skeleton direction, at which the number of edge voxels is maximised.

The length and diameter of selected cells was measured after first calculating the skeleton, using the autoskeleton module in Avizo 9 (FEI VSG, Burlington, MA), and then applying the post-processing techniques described in [35]. The longest-shorted path between skeleton nodes was used to determine cell length, with the length of this path calculated using the multi-seed sphere-network technique [35]. The cell diameter was calculated on planes perpendicular to this path using the modal diameter measure as described above.

3. Results and discussion

The reconstructed slices in Figure 2 show that x-ray nanotomography with Zernike phase contrast can reveal both cell morphology and scaffold structure. Subcellular detail is visible even in these short (~1 hour 37 minutes) scans, in which dose was reduced to avoid the damage occurring to fibres as found for longer scans times (~8 hours). The stitching together of two scans allows the full thickness of the scaffolds to be imaged at 150 nm resolution. However Zernike phase contrast gives rise to halo artefacts around features, which makes image segmentation more difficult. These artefacts were almost all removed by deconvolution with the image filter given in Equation 1. Examples of reconstructed slices before and after phase artefact reduction are shown in Figures 2 (a)-(d). Recently, Kumar *et al.* [36] developed a full model of Zernike phase contrast for Fresnel zone plate x-ray microscopes, allowing the Zernike artefacts to be removed by a similar deconvolution approach. However their model is complex to implement, and regularisation for the deconvolution step requires 8 user-defined parameters to be optimised. In comparison, the approach developed in this paper is simpler and more practical, requiring only one parameter to be optimised.

Segmentation of the cells and fibres facilitates 3-D visualisation of the data as well as quantitative analysis. A 3-D rendering of a scaffold with cells grown for 3 days is given in Figure 4, showing that the majority of the cells are at or close to the upper scaffold surface. Subcellular detail is clearly visible, including the nucleus (see also Figures 2 and 5) and a

texture which may be associated with the cytoskeleton and other organelles. The interplay between cell morphology and fibre arrangement is shown in greater detail in Figure 5 for a single cell at a depth of ~43 μm after culture for 6 days. The fibre arrangement has constricted the growth of the cell such that it takes a tortuous path between fibres, with the cell length being 41.5 μm in comparison to the Euclidean distance across the cell (from skeleton path start and end points, see Section 2.3) being 24.9 μm. The diameter of the cell has also been restricted, with the modal diameter taking values in the range 0.6 to 3.2 μm, with the median value being 1.6 μm.

Surface imaging of cells grown in electrospun scaffolds using SEM has previously been reported [28]. In this study we show that cell migration has occurred across the full thicknesses of the scaffolds, with the thicknesses measured to be in the range 68 to 88 μm. The distribution of cell volume with distance is shown for a single ROI in Figures 6 and overall ROIs in Figure 7. The shape of the histogram is essentially unaffected by segmenting the cells on every 10th slice in comparison to a full segmentation, as shown in Figure 6. The overall distributions provide evidence for greater migration of the cells into the scaffold after 6 days. For example, the proportion of cell volume at a depth of 40 μm or greater increased on average (over the ROIs) from 3.8% to 8.5% (the weighted proportion increased from 3.6% to 7.7%) between 3 days and 6 days. This proportion was significantly greater for 6 days in 69% of pairwise comparisons ($p < 0.024$ for unweighted and $p < 0.0001$ for weighted volumes) between ROIs at the two time points. There is also evident of an increase in cell volume (averaged over the ROIs) by 42 % (t-test, $p < 0.095$), or 53% (t-test, $p < 0.095$) for the weighted volume, between 3 and 6 days. The scaffold architecture was very similar for the ROIs at the two times points, including the porosity (77 ± 5 % for 3 days and 77 ± 3 % for 6 days), the pore space diameter (see Figure 8) and the average fibre diameter, which was measured to be 3.8 ± 0.2 μm for both time points. This suggests that the differences in cell volume and distribution are due to culture time.

However the relatively low cell density for these samples means that the results might not be representative of the scaffolds as a whole. The technique is therefore more suitable for analysing higher cell densities. However, the analysis volume per ROI could be increased by ~60% by stitching together radiographs prior to reconstruction (so that each projection has around twice the field of view along the axis perpendicular to the rotation axis) rather than stitching volumes after reconstruction as was the case in this study.

Overall, it is clear that X-ray phase contrast nanotomography has advantages over 3-D optical techniques, such as LSCM, as more complete information is obtained (rather than just visualisation of labelled structures) and the image resolution and contrast are isotropic across the field of view, which are conducive to quantitative analysis. The main disadvantage is the limited field of view, even when multiple regions are scanned, which makes quantitative analysis of cell infiltration appropriate only when cell densities are high. However, as the technique is non-destructive, it can be combined with complimentary imaging techniques, such microCT or LSCM, in a hierarchical correlative imaging approach to provide information across length scales [9]. In particular X-ray nanotomography could provide a link between optical imaging and much higher resolution destructive SEM imaging techniques, to enable targeted imaging of preselected features [37]. Such a correlative imaging approach would allow multiple growth stages to be studied and allow more in-depth information to be gained on the influence of scaffold architecture, for example by varying porosity. 3-D

imaging of specific cells could be achieved by combining x-ray nanotomography with targeted staining with heavy metals by for example the approach detailed in [16].

4. Conclusions

We have demonstrated that x-ray nanotomography with Zernike phase contrast can be used to image cells in polymer scaffolds at a resolution of 150 nm. The high resolution enables subcellular detail to be obtained whilst making the technique attractive for characterising nano-fibre scaffolds [38]. The scan settings were optimised to reduce scan times and dose while maintaining an acceptable image quality, making feasible the analysis of multiple regions of interest in relatively large samples. An image processing procedure has been developed to enable quantitative characterisation of scaffold architecture as well as determination of cell location and morphology. A proportion of the cells is found to immerse themselves 40μm deep inside the scaffold and they clearly adhere to the polymer surface. This scaffold material is thereby demonstrated to be a favourable growth environment for the cells. The linking together of 3-D information on both cells and scaffold can provide new insights into the interplay between scaffold architecture and cell morphology, cyto-compatibility, seeding efficiency and bioactivity.

Author contributions

RSB performed the xray experiments, measurements and analysis from all the samples. MY conceived the project and prepared the cell/scaffold samples after cell culture. IR and MY provided regular feedback on the project. RSB wrote the manuscript with MY and IR helped in amending the manuscript.

References

1. Chan BP, Leong KW (2008) Scaffolding in tissue engineering: general approaches and tissue-specific considerations. Eur Spine J 17 Suppl 4:467-479. doi:10.1007/s00586-008-0745-3

2. Costantini M, Colosi C, Mozetic P, Jaroszewicz J, Tosato A, Rainer A, Trombetta M, Święszkowski W, Dentini M, Barbetta A (2016) Correlation between porous texture and cell seeding efficiency of gas foaming and microfluidic foaming scaffolds. Materials Science and Engineering: C 62:668-677. doi:http://dx.doi.org/10.1016/j.msec.2016.02.010

3. Barbetta A, Bedini R, Pecci R, Dentini M (2012) Role of X-ray microtomography in tissue engineering. Ann Ist Super Sanita 48 (1):10-18. doi:DOI: 10.4415/ANN_12_01_03

4. Appel AA, Anastasio MA, Larson JC, Brey EM (2013) Imaging challenges in biomaterials and tissue engineering. Biomaterials 34 (28):6615-6630. doi:10.1016/j.biomaterials.2013.05.033

5. Pampaloni F, Reynaud EG, Stelzer EHK (2007) The third dimension bridges the gap between cell culture and live tissue. Nat Rev Mol Cell Biol 8 (10):839-845

6. Al-Abboodi A, Fu J, Doran PM, Chan PPY (2013) Three-dimensional nanocharacterization of porous hydrogel with ion and electron beams. Biotechnology and Bioengineering 110 (1):318-326. doi:10.1002/bit.24612

7. Lamers E, Walboomers XF, Domanski M, McKerr G, O'Hagan BM, Barnes CA, Peto L, Luttge R, Winnubst LA, Gardeniers HJ, Jansen JA (2011) Cryo DualBeam Focused Ion Beam-Scanning Electron Microscopy to Evaluate the Interface Between Cells and Nanopatterned Scaffolds. Tissue Eng Part C Methods 17 (1):1-7. doi:10.1089/ten.TEC.2010.0251

8. Wierzbicki R, Købler C, Jensen MRB, Łopacińska J, Schmidt MS, Skolimowski M, Abeille F, Qvortrup K, Mølhave K (2013) Mapping the Complex Morphology of Cell Interactions with Nanowire Substrates Using FIB-SEM. PLoS ONE 8 (1):e53307. doi:10.1371/journal.pone.0053307

9. Bradley RS, Withers PJ (2016) Correlative multiscale tomography of biological materials: challenges and opportunities. MRS Bullitin Accepted for publication

10. Peyrin F (2011) Evaluation of bone scaffolds by micro-CT. Osteoporosis International 22 (6):2043-2048. doi:10.1007/s00198-011-1609-y

11. Westhauser F, Weis C, Hoellig M, Swing T, Schmidmaier G, Weber MA, Stiller W, Kauczor HU, Moghaddam A (2015) Heidelberg-mCT-Analyzer: a novel method for standardized microcomputed-tomography-guided evaluation of scaffold properties in bone and tissue research. R Soc Open Sci 2 (11):150496. doi:10.1098/rsos.150496

12. Wu X, Wang L, Deng F, Watts DC (2014) Mouse calvarial defect Model: An approach for the micro-tomographic evaluation of polymer scaffolds. Microscopy Research and Technique 77 (12):1037-1043. doi:10.1002/jemt.22433

13. Papantoniou I, Sonnaert M, Geris L, Luyten FP, Schrooten J, Kerckhofs G (2014) Three-Dimensional Characterization of Tissue-Engineered Constructs by Contrast-Enhanced Nanofocus Computed Tomography. Tissue Engineering Part C, Methods 20 (3):177-187. doi:10.1089/ten.tec.2013.0041

14. Dorsey SM, Lin-Gibson S, Simon Jr CG (2009) X-ray microcomputed tomography for the measurement of cell adhesionand proliferation in polymer scaffolds. Biomaterials 30 (16):2967-2974. doi:http://dx.doi.org/10.1016/j.biomaterials.2009.02.032

15. Bosworth LA, Rathbone SR, Bradley RS, Cartmell SH (2014) Dynamic loading of electrospun yarns guides mesenchymal stem cells towards a tendon lineage. Journal of the Mechanical Behavior of Biomedical Materials 39:175-183. doi:10.1016/j.jmbbm.2014.07.009

16. Zehbe R, Goebbels J, Ibold Y, Gross U, Schubert H (2010) Three-dimensional visualization of in vitro cultivated chondrocytes inside porous gelatine scaffolds: A tomographic approach. Acta Biomaterialia 6 (6):2097-2107. doi:http://dx.doi.org/10.1016/j.actbio.2009.11.020

17. Thimm BW, Hofmann S, Schneider P, Carretta R, Müller R (2011) Imaging of Cellular Spread on a Three-Dimensional Scaffold by Means of a Novel Cell-Labeling Technique for High-Resolution Computed Tomography. Tissue Engineering Part C: Methods 18 (3):167-175. doi:10.1089/ten.tec.2011.0262

18. Shearer T, Rawson S, Castro SJ, Balint R, Bradley RS, Lowe T, Vila-Comamala J, Lee PD, Cartmell SH (2014) X-ray computed tomography of the anterior cruciate ligament and patellar tendon. Muscles, Ligaments and Tendons Journal 4 (2):238-244

19. Thurner P, Müller R, Raeber G, Sennhauser U, Hubbell JA (2005) 3D morphology of cell cultures: A quantitative approach using micrometer synchrotron light tomography. Microscopy Research and Technique 66 (6):289-298. doi:10.1002/jemt.20170

20. Appel A, Anastasio MA, Brey EM (2011) Potential for Imaging Engineered Tissues with X-Ray Phase Contrast. Tissue Engineering Part B, Reviews 17 (5):321-330. doi:10.1089/ten.teb.2011.0230

21. Voronov RS, VanGordon SB, Shambaugh RL, Papavassiliou DV, Sikavitsas VI (2012) 3D Tissue-Engineered Construct Analysis via Conventional High-Resolution Microcomputed Tomography Without X-Ray Contrast. Tissue Engineering Part C: Methods 19 (5):327-335. doi:10.1089/ten.tec.2011.0612

22. Takashima K, Hoshino M, Uesugi K, Yagi N, Matsuda S, Nakahira A, Osumi N, Kohzuki M, Onodera H (2015) X-ray phase-contrast computed tomography visualizes the microstructure and degradation profile of implanted biodegradable scaffolds after spinal cord injury. Journal of Synchrotron Radiation 22 (Pt 1):136-142. doi:10.1107/S160057751402270X

23. Hagen CK, Maghsoudlou P, Totonelli G, Diemoz PC, Endrizzi M, Rigon L, Menk R-H, Arfelli F, Dreossi D, Brun E, Coan P, Bravin A, De Coppi P, Olivo A (2015) High contrast microstructural visualization of natural acellular matrices by means of phase-based x-ray tomography. Scientific Reports 5:18156. doi:10.1038/srep18156

24. Stampanoni M, Mokso R, Marone F, Vila-Comamala J, Gorelick S, Trtik P, Jefimovs K, David C (2010) Phase-contrast tomography at the nanoscale using hard x rays. Physical Review B 81 (14):140105

25. Yang Y, Li W, Liu G, Zhang X, Chen J, Wu W, Guan Y, Xiong Y, Tian* Y, Wu* Z (2010) 3D visualization of subcellular structures of Schizosaccharomyces pombe by hard X-ray tomography. Journal of Microscopy 240 (1):14-20. doi:10.1111/j.1365-2818.2010.03379.x

26. Mokso R, Quaroni L, Marone F, Irvine S, Vila-Comamala J, Blanke A, Stampanoni M (2012) X-ray mosaic nanotomography of large microorganisms. Journal of Structural Biology 177 (2):233-238. doi:http://dx.doi.org/10.1016/j.jsb.2011.12.014

27. Diaz A, Malkova B, Holler M, Guizar-Sicairos M, Lima E, Panneels V, Pigino G, Bittermann AG, Wettstein L, Tomizaki T, Bunk O, Schertler G, Ishikawa T, Wepf R, Menzel A (2015) Three-dimensional mass density mapping of cellular ultrastructure by ptychographic X-ray nanotomography. Journal of Structural Biology 192 (3):461-469. doi:http://dx.doi.org/10.1016/j.jsb.2015.10.008

28. Yusuf M, Millas ALG, Estandarte AKC, Bhella GK, McKean R, Bittencourt E, Robinson IK (2014) Platinum blue staining of cells grown in electrospun scaffolds. Biotechniques 57 (3):137-141

29. Millas ALG, McKean R, Stevens R, Yusuf M, Silveira JVW, Puzzi MB, Bittencourt E (2014) Fabrication of Electrospun Scaffolds Incorporating an Amazonian Therapeutic Oil from the Copaifera Species for Wound Care Applications. Journal of Biomaterials and Tissue Engineering 4 (3):217-220. doi:10.1166/jbt.2014.1162

30. Tkachuk A, Duewer F, Cui H, Feser M, Wang S, Yun W (2007) X-ray computed tomography in Zernike phase contrast mode at 8 keV with 50-nm resolution using Cu rotating anode X-ray source. Zeitschrift Fur Kristallographie 222, Issu 11:650-655

31. Yin Z, Kanade T, Chen M (2012) Understanding the Phase Contrast Optics to Restore Artifact-free Microscopy Images for Segmentation. Medical Image Analysis 16 (5):1047-1062. doi:10.1016/j.media.2011.12.006

32. Chan SH, Khoshabeh R, Gibson KB, Gill PE, Nguyen TQ (2011) An Augmented Lagrangian Method for Total Variation Video Restoration. IEEE Transactions on Image Processing 20 (11):3097-3111. doi:10.1109/TIP.2011.2158229

33. Dougherty R, Kunzelmann K-H (2007) Computing Local Thickness of 3D Structures with ImageJ. Microscopy and Microanalysis 13 (SupplementS02):1678-1679. doi:doi:10.1017/S1431927607074430

34. Hildebrand T, Rüegsegger P (1997) A new method for the model-independent assessment of thickness in three-dimensional images. Journal of Microscopy 185 (1):67-75. doi:10.1046/j.1365-2818.1997.1340694.x

35. Bradley RS, Withers PJ (2016) Post-processing techniques for making reliable measurements from curve-skeletons. Computers in Biology and Medicine 72:120-131. doi:http://dx.doi.org/10.1016/j.compbiomed.2016.03.008

36. Kumar AS, Mandal P, Zhang Y, Litster S (2015) Image segmentation of nanoscale Zernike phase contrast X-ray computed tomography images. Journal of Applied Physics 117 (18):183102. doi:doi:http://dx.doi.org/10.1063/1.4919835

37. Burnett TL, McDonald SA, Gholinia A, Geurts R, Janus M, Slater T, Haigh SJ, Ornek C, Almuaili F, Engelberg DL, Thompson GE, Withers PJ (2014) Correlative Tomography. Scientific Reports 4:4711. doi:10.1038/srep04711

38. Kanani AG, Bahrami SH (2010) Review on electrospun nanofibers scaffold and biomedical applications. Trends Biomater Artif Organs 24 (2):93-115
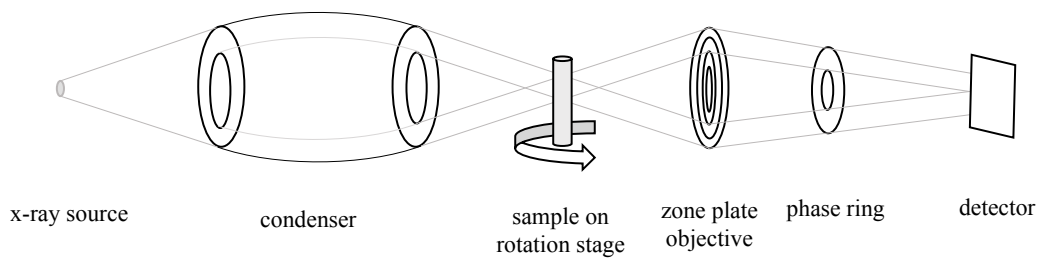
Figure 1. Schematic diagram of a transmission x-ray microscope with Zernike phase contrast. The x-ray paths are shown in grey and phase contrast is achieved via the phase ring placed in the back focal plane of the zone plate objective.
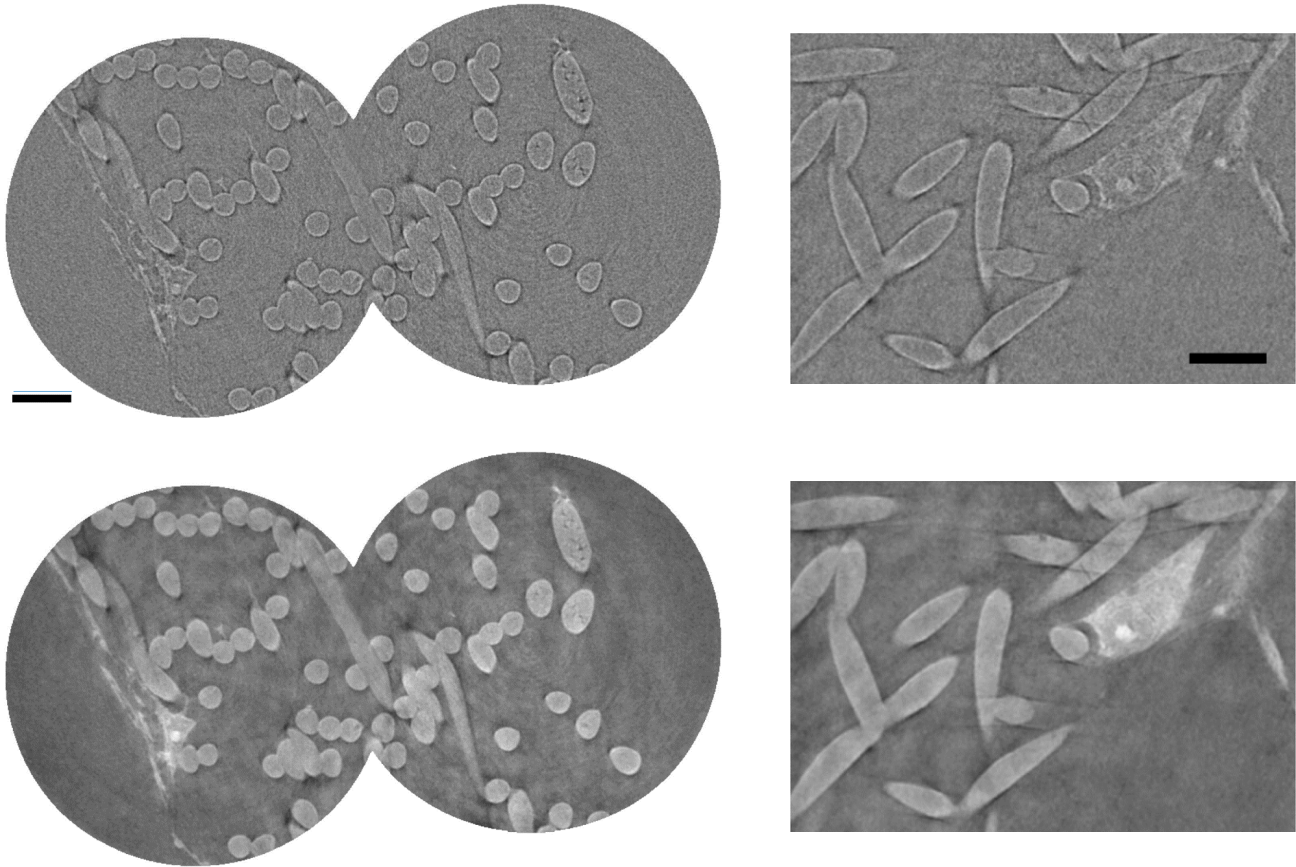
Figure 2. (a) Reconstructed slice through a scaffold after stitching together 2 scans. The upper scaffold surface is on the left hand side. Scale bar is 15 μm. (b) Enlarged section of a slice showing a cell subcellular detail clearly visible. Scale bar is 15 μm. The corresponding slices after phase artefact removal are shown in (c) and (d).
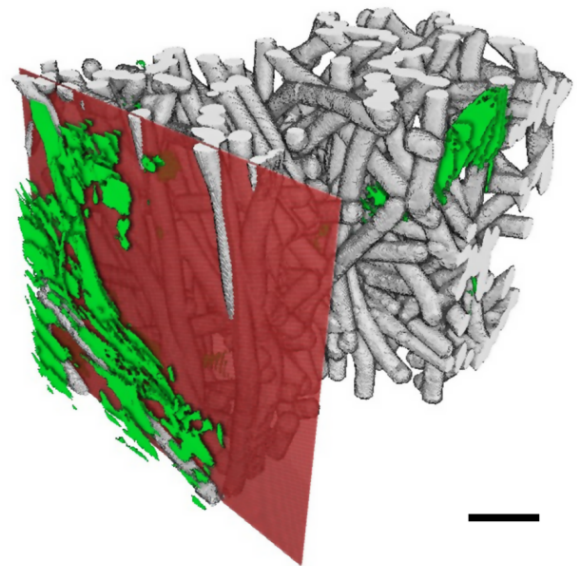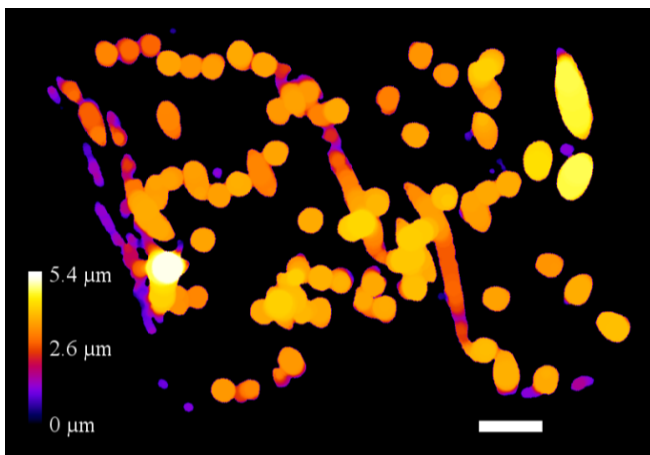
Figure 3. (a) Local thickness map used in step 3 of the segmentation process (see Section 2.3) shown for the slice in Fig 2(a). Scale bar is 10 μm. (b) 3-D rendering of the segmented data with fibres in grey and cells in green. The 2-D plane fitted to the upper scaffold surface is shown in red. Scale bar is 20 μm.
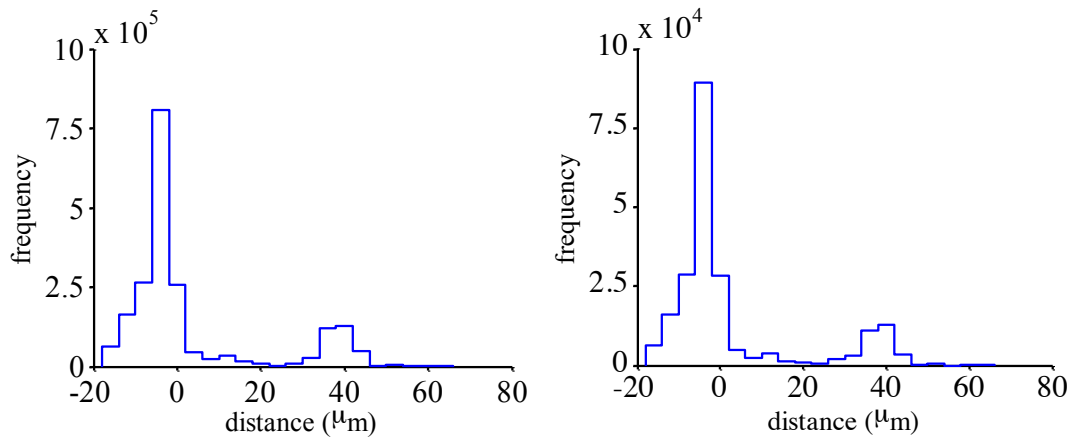
Figure 4. Distribution of the number of cell voxels as a function of distance for (a) full cell segmentation and (b) segmentation on every 10th slice for a scaffold with cells grown for 3 days.
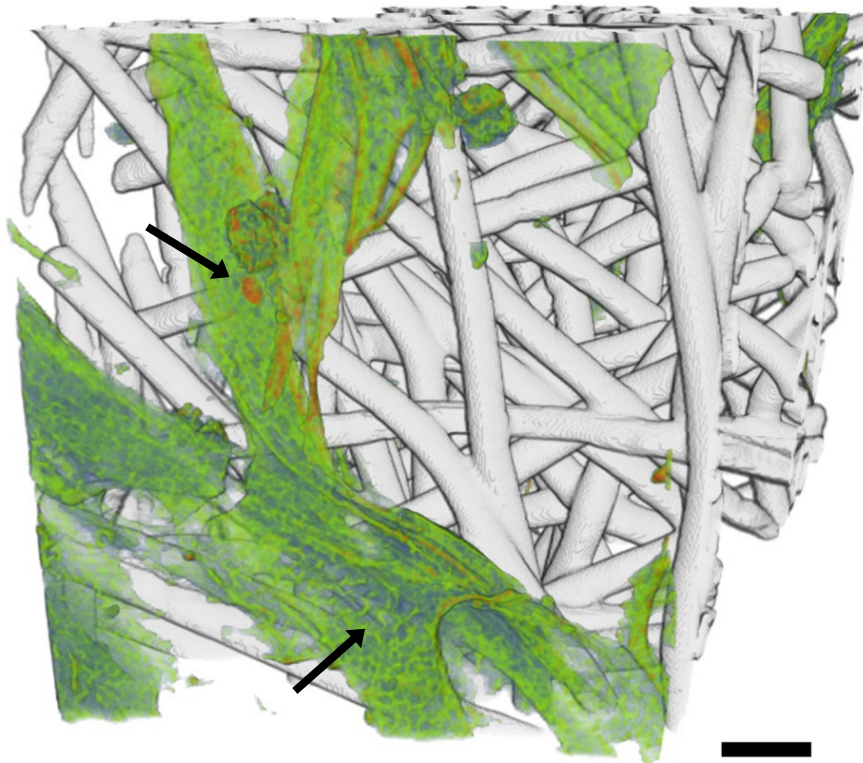
Figure 5. 3-D rendering showing cells distributed on and within the scaffold after being grown for 3 days. Subcelluar details is evident, including the nucleus (marked with an arrow and shown in red) and texture associated with the cytoskeleton?! YUSUF – PLEASE CHECK (bottom arrow – is this necessary?). Scale bar is 10 μm.
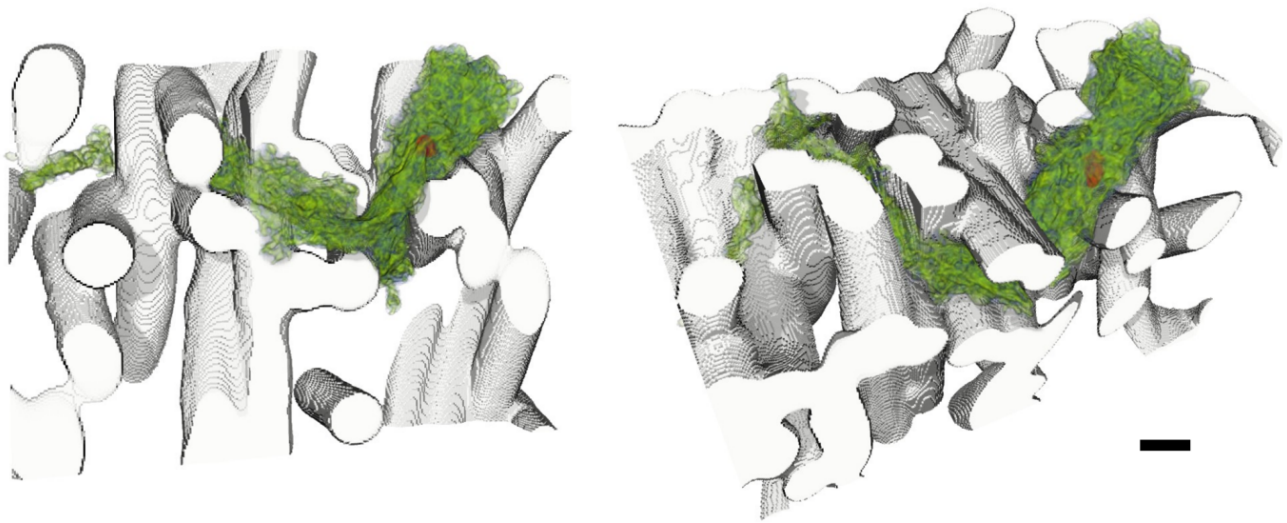
Figure 6. 3-D renderings of a cell located at ~43 µm into a scaffold after culturing for 6 days. The cell morphology is clearly influenced by the local distribution of fibres and their orientation. The cell nucleus is shown in red. Scale bar is 3 µm.
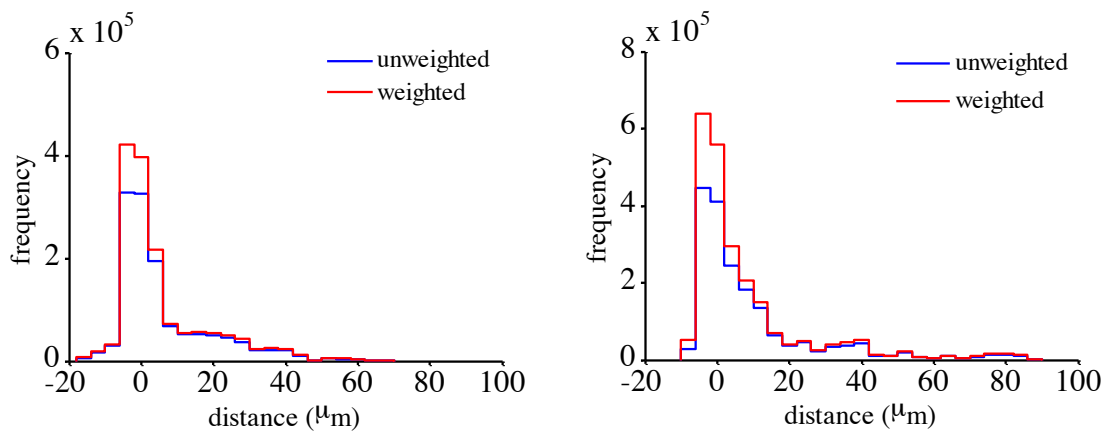
Figure 7. Net distribution over 6 ROIs of the number of cell voxels as a function of distance from the upper scaffold surface for (a) 3 days and (b) 6 days. The distributions are shown before and after weighting was applied to account for the non-uniform sampling as a function of distance (see Section 2.3)
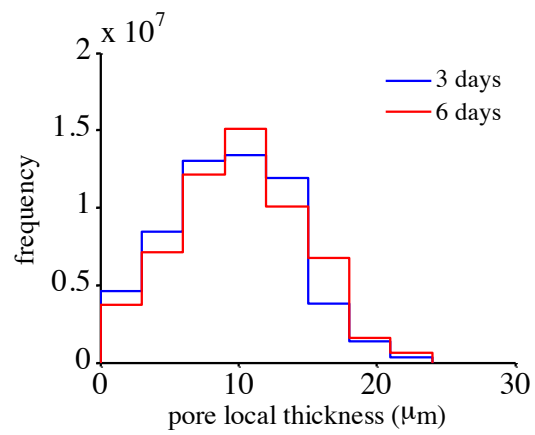
Figure 8. Local thickness distribution of the scaffold pore space for 3 and 6 days. The mean local thickness is 10.9 ± 4.5 μm and 11.5 ± 4.6 μm for 3 and 6 days, respectively.